

3D Magnetic Field Reconstruction with Magnetoresistive Sensors

Filipe Masuch Ribeiro Richheimer^{1,2,*}

¹*Department of Physics, Instituto Superior Técnico,*

Universidade de Lisboa, Av. Rovisco Pais 1, 1049-001 Lisboa, Portugal

²*Instituto de Engenharia de Sistemas de Computadores - Microsystems and Nanotechnology (INESC-MN),*

Rua Alves Redol 9, 1000-029 Lisboa, Portugal

The use of scanning magnetoresistive microscopes (SMRM) as magnetic imaging devices is a very promising method compared to other widely used methods such as magnetic force microscopy, due to the ability to perform direct measurements in ambient conditions. A SMRM setup using a spin valve sensor integrated in an atomic force microscopy cantilever was studied experimentally, providing an understanding of the influence of electrical and mechanical parameters on the response to external fields, together with an identification of the optimal settings for magnetic imaging outputs. In addition, a computational model replicating the sensor response was developed. The studies are focused on the measurement of a set of micrometric permanent magnet CoFe sample arrays with in-plane magnetization. Combining the experimental and computational results, an algorithm was developed to quantify the magnetization orientation by successive comparison with simulations of incrementally rotated magnetization direction generated by the computational model. The corrected magnetization orientations were fed as input parameters to allow the simulation to replicate the experimental reality. Combining the previous results, we were able to perform a 3D magnetic field reconstruction by measuring the same sample structures along different sensitive directions, allowing us to reconstruct the cartesian components of the sample stray field by a linear system of equations after describing geometrically the orientation of the sensitive sensor axis.

Keywords: Magnetic field reconstruction, Spin valve, Scanning magnetoresistive microscopy, In-plane magnetization, Magnetic stray field

I. INTRODUCTION

In modern micro- and nanotechnology, device properties are not only dependent on the material composition but also on the size and shape [1][2][3]. Thus, it is of utmost importance to be able to relate to structural properties even when characterizing other physical quantities of a sample in the micro- to nanometer length scales. One important physical property used in micro- and nanotechnology is magnetism, in form of recording media for hard disk drives, magnetic random access memories [4][5] or magnetic nanoparticle tagging for biological applications [6][7], in DNA [8] or cancer cells [9].

The most common magnetic imaging tool presently is magnetic force microscopy (MFM), bringing the advantage of high resolution and no need of sample preparation, nonetheless it is only sensitive to magnetic field gradients and not the magnetic field itself, additionally to the fact that lateral magnetizations are difficult to detect, as the tip measures force interactions through vertical tip deflection[10].

A characterization tool that offers to combine state-of-the-art magnetoresistive imaging with simultaneous topography mapping is given with scanning magnetoresistive microscopy (SMRM), where magnetoresistive sensors are integrated in microfabricated atomic force microscopy (AFM) cantilevers. The use of magnetoresistive sensors for stray field mapping compared to field detection through magnetized probe

tips in MFM brings the advantage of direct magnetic field measurements along a uniaxial sensitive direction. As this work will show, by correct application of the sensing orientation, 3D magnetic field reconstruction with a single sensor can be achieved. Moreover, the AFM setup allows to give insight on the sample structure through topography maps, providing the desired interconnection of topographic characterization when studying physical properties of micro- and nanometric samples.

A. Objectives and Outline

This work is focused on the study of a GMR sensor integrated in a microfabricated AFM cantilever is on a previously assembled experimental setup [10] and is structured according the three major milestones projected to be achieved. The first chapter of the main thesis development provides a detailed study of the influence of experimental, electronic and mechanical, setup parameters on the magnetic imaging scanning results, finishing with the fundamented presentation of optimal setup parameters for further experimental studies.

Next, an experimental evaluation of the experimental work will be performed, involving the study of noise and offset types affecting the magnetic imaging results. Additionally, we will implement sample measurements in an adapted measurement routine to be able to achieve a 3D magnetic field decomposition with a single sensor magnetic field sensitivity axis.

Finally, a computational implementation of the experimental setup will be reproduced, focusing on the magnetic stray field generation of micrometric rect-

*Electronic address: filipe.richheimer@tecnico.ulisboa.pt

angular permanent magnet sample arrays and the resulting response of a sensor with non negligible dimensions. This implementation will simultaneously allow validation of experimental results and physical interpretation of the measured sample patterns. Moreover, a prediction of magnetic imaging outputs with different sensor geometries will be made.

II. THEORETICAL BACKGROUND

A. Magnetoresistive Field Sensors

1. Giant Magnetoresistance

The GMR mechanism is based on the spin dependent scattering rates, which can be originated by a variety of sources, such as impurities or defects [11]. An additional aspect is the presence of ferromagnet/nonmagnet interfaces. The difference in band structures of adjacent layers will give rise to spin-dependent interfacial resistances, where the matching favors the majority electrons due to reduced potential steps at the interfaces [12]. However, the dominant physical effects at the interfaces will depend to the orientation of the applied electric field and hence the electric current, which in GMR devices can be applied either perpendicular to the plane (CPP) or in plane (CIP), where by planes we denote the planes of layers of magnetic and nonmagnetic materials.

2. Spin Valve Device

The most basic spin valve configuration, F1-N-F2-AF, comprises of a non-magnetic spacer layer (NM) of typically ~ 2 nm, sandwiched by two ferromagnetic layers (F1, F2). By pinning one of the layers (F2) through an adjacent antiferromagnetic (AF) layer using the exchange bias [13], F1 remains as a so-called free layer, meaning that its magnetization orientation can be easily manipulated by an applied external magnetic field, which has to be weak enough not to break the coupling of the exchange anisotropy fixing the pinned layer.

The maximum resistance of the above mentioned device will be achieved when the free layer is perpendicular to the pinned layer, R_{AP} achieving the minimum state when both layers are parallel, R_P . Upon application of an external field, the free layer magnetic moment of the free layer M_1 directs itself along the field, changing the resistance of the device.

When designing a SV, the choice of materials and the thickness has an impact on the resulting MR ratio as well as on the $R(H)$ transfer curve resulting from the device. For sensor applications, one important property is a linearized sensor output (transfer curve). This is achieved by setting the magnetization orientation of free and pinned layer orthogonal during deposition making use of the magnetocrystalline

anisotropy [14]. Each crystalline structure has a favored natural orientation determined by the principal axes, which therefore also determines the favored magnetization orientation (easy axis) in the case of a ferromagnet. The energy cost of moving the magnetization away from that orientation is given by the magnetocrystalline anisotropy energy. An orthogonal orientation between free and pinned layer will mean that at zero external field the sensor lies at an intermediate resistance state. For an unshielded spin valve sensor, the voltage output can be given by [15]

$$\Delta V = \frac{1}{2} MR R_s I \left(\frac{L}{W} \right) < \cos(\theta_f - \theta_p) >, \quad (1)$$

where MR is the device magnetoresistance ratio, R_s is the device sheet resistance, I the applied CIP current, L the sensor dimension along the long axis, W the dimension along the short axis and θ_f and θ_p are the angle of the free and pinned layer magnetization towards the longitudinal axis. In order to achieve linearized outputs for sensor applications the angles of the free and pinned layer at zero external field should be $\theta_f = 0^\circ$ and $\theta_p = 90^\circ$.

Apart from the relative orientation, magnetic coupling interactions inbetween layers in a SV play an important role on the output signal of the device and hence the resulting transfer curve. The exchange bias describes the coupling between the pinned and antiferromagnetic layer in order to achieve an unidirectional orientation of the pinned layer. The effect of this interaction is a horizontal shift in the sensor transfer curve. Another coupling interaction, the interlayer coupling, joins all the couplings between ferromagnetic layers with different physical origins, as magnetostatic coupling, Néel coupling [16] or RKKY coupling. These interactions equally introduce offsets in the device transfer curve.

One strategy to reduce the magnetostatic coupling between pinned and free layers is the introduction of a synthetic antiferromagnet (SAF) structure, where an additional ferromagnetic layer is antiferromagnetically coupled to the pinned layer using RKKY coupling, usually separated by a subnanometrically thick Ru layer [17]. Moreover, the antiparallel coupling of the SAF is more robust to external fields than the exchange bias of AF/F, meaning that less torque from a rotating pinned layer is exerted on the free layer.

To summarize the brief discussion on the basic principles in SV design for sensing applications, we present a visualization of the active layers in a magnetic field sensor based on a SV device with a SAF structure including the main interlayer interactions in Fig. 1.

B. Scanning Probe Microscopy

Scanning probe microscopy (SPM) is one of the fundamental tools in nanotechnology, based on the the characterization of a sample structure by scanning a bidimensional area using a probe tip with sharpness

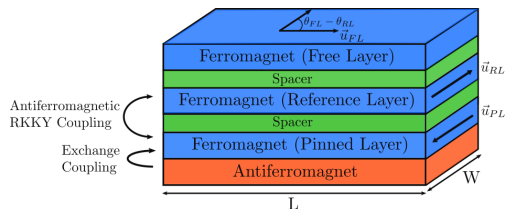


FIG. 1: Scheme of a typical SV structure for sensor applications.

down to the atomic scale. The characterization is performed by the evaluation of forces interacting between the sample and the tip, allowing to study several physical properties, ranging from topography to magnetic field strength.

1. Scanning Tunneling Microscopy

One of the first SPM methods was invented in 1982, where Binnig and Rohrer reported the first experimental results in scanning tunneling microscopy (STM) [18]. In this technique, a voltage is applied between a probe tip and an electrical conductor sample. By maintaining the tip close to the sample, electrons are able to tunnel from occupied electronic states of the tip into empty states of the sample. However, this method had a limited range of applicability, since only electrically conducting samples are able to be characterized.

STM measurements can be executed usually in two distinct modes, the constant current mode and the constant height mode. In the constant current mode, the measured tunneling current is maintained constant by adjusting the height of the probe tip with a feedback control mechanism, with the advantage that the measured signal is kept in a desired range.

2. Atomic Force Microscopy

In atomic force microscopy (AFM), interatomic forces between a microfabricated sharp tip and a sample surface are measured. During the scanning process, the interaction of the tip and the sample surface is detected by the deflection of a cantilever spring the tip is mounted to. The deflection is detected through a laser that focuses a mirror attached to the cantilever, deflecting the beam towards a position sensitive photosensor. A typical schematic of an AFM setup is presented in figure [2].

The fundamental principle of the interaction between the AFM tip and the sample is the atom-atom interaction that can be described by a Lennard-Jones type potential of the type:

$$V_{LJ}(d) = -4\epsilon \left[\left(\frac{\sigma}{d} \right)^6 - \left(\frac{\sigma}{d} \right)^{12} \right] \quad (2)$$

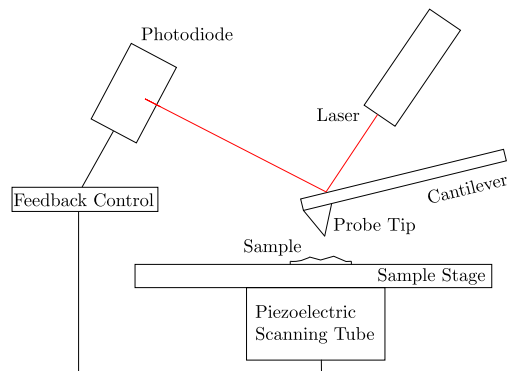


FIG. 2: Atomic force microscope schematic.

where σ and ϵ are material dependent intrinsic parameters and d is the interatomic distance. In figure [3] a representation of V_{LJ} as a function of d is made.

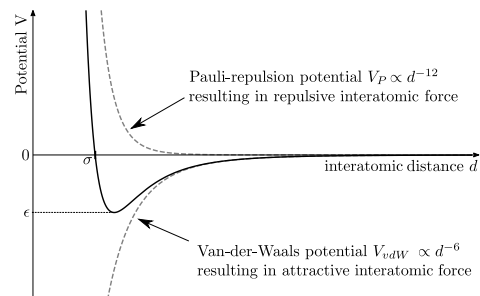


FIG. 3: Two atom interaction Lennard-Jones potential.

The Lennard-Jones potential is made of two terms, an attractive term resulting from a negative potential and a repulsive term resulting from a positive potential. The attractive term has a longer range action and is caused by van-der-Waals interactions proportional to $V_{vdW} \propto d^{-6}$. The repulsive term is short-ranged and appears when atoms are sufficiently close for orbitals of each atom to overlap, causing the Pauli exclusion principle to act. This term is proportional to $V_P \propto d^{-12}$. In an AFM tip, hundreds of atoms interact with the sample surface, meaning that corrections on the Lennard-Jones potential have to be made, taking into account interactions on multiple atoms, as well as the shape of the tip. A detailed explanation on the different types of corrections can be found in [19].

AFM measurements can be operated in two distinct modes, either in contact (static) or in tapping (dynamic) mode. When running in contact mode, the tip is brought into direct contact with the sample, meaning that the measurements take place in the repulsive regime of the interaction potential. This method has a less complex implementation and is therefore widely used, having the disadvantage that the continuous force applied by the tip on the sample combined with the dragging movement of the scan might damage soft tissues samples [20]. Additionally, this method is prone to lateral forces that can modify and distort the scans [21] In dynamic mode AFM measure-

ments the cantilever is brought into forced oscillatory movement close to the resonant frequency, interacting with the sample surface by a tapping movement. As a result, amplitude and phase results of the cantilever deflection can be studied separately, allowing to extract different physical properties of the sample [22]. This allows to study more sensitive surfaces, however the interaction forces and therefore displacements are significantly smaller as this method operates in the attractive potential regime, decreasing the resolution of the imaging results [23].

III. EXPERIMENTAL AND NUMERICAL IMPLEMENTATION

A. Experimental Implementation

1. Integrated Device Properties

The $19.5\mu\text{m}$ long and $2.5\mu\text{m}$ wide SV sensor is embedded at the tip of a $456\mu\text{m}$ long and $69\mu\text{m}$ wide Si cantilever with its long axis perpendicular to the cantilever direction, as it is shown in figure [4]. The stack was composed by $2\text{ Ta}/3\text{ Ni}_{80}\text{Fe}_{20}/8.5\text{ Mn}_{78}\text{Ir}_{24}/2.3\text{ Co}_{80}\text{Fe}_{20}/0.8\text{ Ru}/2.3\text{ Co}_{80}\text{Fe}_{20}/2.7\text{ Cu}/2.3\text{ Co}_{80}\text{Fe}_{20}/3.6\text{ Ni}_{80}\text{Fe}_{20}/5\text{ Ta}$, where the values in front of the chemical composition correspond to the thickness of each layer in nanometers.

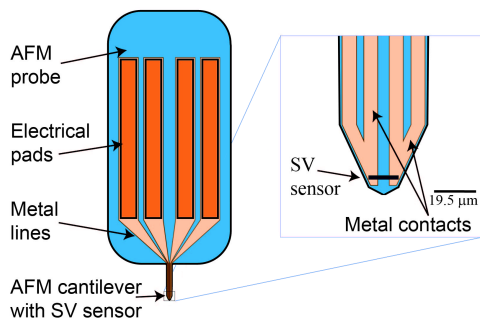


FIG. 4: Cantilever schematic. Taken from [24]

The mechanical and electrical properties of the cantilever were previously determined by the MEMS group at INL, obtaining a resonance frequency of $f_{\text{res}} = 31.1\text{kHz}$ and a spring constant $k = 3.36\frac{\text{N}}{\text{m}}$. The electrical properties of the SV sensor were studied through its response when placed inside a uniform magnetic field generated by Helmholtz coils, allowing to derive a electric resistance $R = 150\Omega$, a magnetoresistance ratio $\text{MR} = 5.49\%$ and a sensitivity $\frac{dV}{dH} = 85.60\frac{\text{V}}{\text{Oe}}$.

2. Scanning System

The scanning system used in this work is a commercial, however customized AFM system developed by *Nanosurf*, which accommodates electronics capable of simultaneously processing topography data and MR sensor signals. The AFM head has a two dimensional scan range of $100\mu\text{m}$ on each axis with a drive resolution of 1.53nm on the x - y plane and approximately 10 times smaller along the z axis with 0.15nm . A translation stage is attached to the head with a travel range of 13mm in each spatial direction, having a repositioning precision and straight line accuracy both below $10\mu\text{m}$. When the cantilever is mounted on the AFM head, it has an angular elevation of 10° towards the x - y sample plane that will allow the sensitive direction of the sensor to capture contributions, as we will see in upcoming sections, of each of the three Cartesian magnetic field components. The AFM measurements in this work will be executed in contact and constant force mode. Thus, two different measurements will be provided separately, the Topography methods corresponding to the height compensations to maintain the tip-sample interactions constant and the Deflections, measuring the instantaneous cantilever deflection at each point.

3. Electronic Setup

The electronic setup was designed by the MEMS group at INL and consists of a closed circuit between an AC current source connected to a variable resistance and the sensor head in series. A visual representation of the circuit is presented in fig. 5. At each

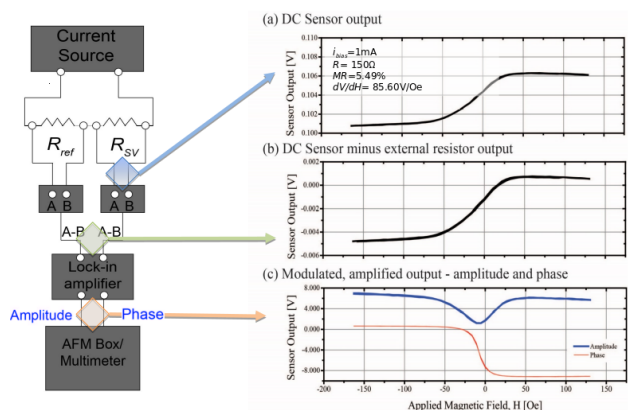


FIG. 5: Effects of the electronic setup on the MR signal. Taken from [24]

relevant circuit node, the profile of the sensor transfer curve is presented. The transfer curve was generated by placing the sensor inside a coil producing a constant magnetic field. The strength of the generated magnetic field was controlled by the DC current intensity fed to the coil. The first node, corresponding to the blue arrow, shows the DC voltage output com-

ing directly out of the sensor fed with a 1 mA AC bias current. The green arrow points to the transfer curve after removing the voltage offset caused by the internal resistance of the sensor using a nominal resistance connected in series, subtracting both signals in order to zero the signal before amplifying the voltage output. When the zeroed signal enters the lock-in amplifier, the AC signal is decomposed into Amplitude and Phase signals by comparing the sensor output signal with its AC bias current. The transfer curves after lock-in amplification are highlighted by the red arrow. The phase signal shows a very smooth transition from a saturated in-phase behavior to a saturated out of phase regime. This is not expected, as in the lock-in decomposition the phase encodes the sign of the signal, hence expected to be a sharp transition. The measurements of the transfer curves in Fig. 5 were acquired using an AC sensor bias current at 50 kHz. Frequency dependent noise of other circuit components were assumed to be responsible for the distortion of the phase signal, motivating a more detailed analysis regarding the bias frequency.

B. Computational Implementation

The computational implementation has two essential contributions, on one hand the sensor response as a function of a spacial external magnetic field and the sample as the stray field source.

1. Sensor Model

The numerical implementation is focused on replicating the response of a field sensor according to its physical properties. Our model needs to return the magnetic field along a sensitive axis, which in the case of SV sensors is usually defined by the orientation of the reference layer, fixed in a direction perpendicular to the sensor long axis.

As the samples studied in this work will be of the order of magnitude of the sensor, we need to take into account its dimensions. The measured field along the sensitive direction is assumed to be average over the sensor volume of the external magnetic field:

$$B_{\text{avg}} = \frac{1}{V} \int_V (\vec{B} \cdot \vec{n}) dV \quad (3)$$

In addition, the sensor displacement towards the tip has to be taken into account, as well as the orientation of the sensor inside the cantilever. The distance of the sensor center to the cantilever tip in this work is $d = 11.4 \mu\text{m}$ along the cantilever long axis, with the sensor long axis placed transverse to the long axis of the cantilever. Tilt of the cantilever towards the sample plane is $\theta = 10^\circ$. In the upcoming section the spatial 3D fields produced by the samples will be derived which are needed to be fed in the averaging equation along the sensitive axis. This integration is performed numerically using *Mathematica* [25].

2. CoFe sample implementation

In this work, micrometric CoFe magnets with rectangular basis of different dimensions will be studied. Hence, a numerical implementation of the stray fields caused by rectangular bar magnets is needed. The magnetization is assumed to be oriented in the lateral plane without vertical component. The stray field distribution was derived using the charge model for permanent magnets [26]. When simulating the scan of multiple magnets inside the scanning area, the spatial field is given by the sum of the fields produced by the sum of the stray fields of each individual magnet.

IV. CALIBRATION

This section is focused on the study of influence of several electronic and mechanical parameters on the output of the magnetic imaging system. Additionally, the first magnetic imaging results with the previously identified parameters are presented and treated.

A. Electrical Setup Parameters Choice

The first part will be focused on the study of the effect of the electrical parameters on the sensor transfer curves. The first parameter for study is the frequency of the AC bias current of the sensor, motivated by the smooth transition of the phase curve which was already discussed. In order to evaluate the effect of the bias frequency on the transfer curves, the sensor was exposed to a constant magnetic field generated by a solenoid while being fed with AC frequencies between 1 Hz and 100 kHz, with the results presented in Fig. 6.

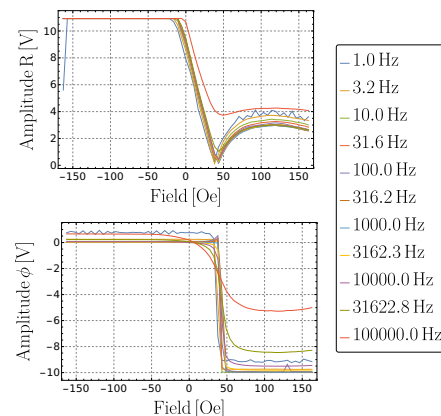


FIG. 6: Raw calibration curves.

In order to evaluate the optimal bias frequency, two requirements have to be taken into account. On one hand the phase curve at the optimal frequency should have a sharp transition from in-phase and out of phase behavior, while on the other hand the frequency should be as high as possible, since the duration of an

acquisition is proportional to the bias frequency. Two criteria were used to identify the bias frequency at which the shape of the phase curve transitioned from sharp to smooth in to out of phase behaviour. On one hand it was observed that the magnitude difference of the saturated plateaus reduced with higher frequencies, furthermore the steepness of the transition reduced, which could be quantified by the absolute of the derivative. Applying both of these methods, we concluded that the limit frequency at which the transition was still sharp was $f = 1$ kHz.

After setting the bias frequency, the lock-in amplifier parameters were studied, namely the sensitivity (amplification amplitude) and the integration time. In a matrix-like approach, we acquired amplitude and phase transfer curves ranging from $300 \mu\text{s}$ to 30 ms in integration time and 1 mV to 10 mV in sensitivity. Very low integration times did not return stable results, while high integration times meant elevated scanning times, as a result, 10 ms was concluded to be the best parameter. For the sensitivity, amplifications between 2 mV and 5 mV were found to be optimal, as higher values exceeded the saturated signal and therefore reducing the gain of the amplification, while lower sensitivities saturated the signal earlier and hence reducing the effective magnetic field bandwidth that could be calibrated using the resulting transfer curves.

B. Mechanical Setup Parameters Choice

The critical parameter of the scanning system that had to be analyzed was the scanning duration of a line in the raster scan, which we will call scanning speed. We note that it was important to consider that the increase of the scanning speed would result in a directly proportional increase of the total scanning duration. As along all of the upcoming work, a fixed square area of $100 \mu\text{m}$ was scanned, acquiring 512 points per line and column. While repeating the same area scan for scanning speed ranging from 0.21 s to 10.0 s, we concluded that 1.0 s was the time/line speed that provided the most balanced results between minimal total scanning durations while providing saturated amplitude results with low spatial phase shift between forward and backwards acquisitions.

The results of the optimal parameter studies are summarized in Tab. I.

Parameter	Value
Bias Current Frequency [Hz]	1000
Integration Time [ms]	10
Lock-In Sensitivity [mV]	5 (2)
Time/Line [s]	1

TABLE I: Concluded parameter summary.

C. Samples and Measurement Procedures

In this section we will give a brief overview of the magnetic samples used in the present magnetic imaging studies in addition to a brief description of the measurement procedures in order to be able to perform 3D magnetic field reconstructions.

In regard to the samples used for this work, a sample mask of different sized multilayered features was available. Each feature is composed of a multilayer stack including an 11 nm thick CoFe layer for permanent magnetization. All the features were coherently magnetized along the x -axis. The basis dimensions of the cuboidal feature arrays ranged from $1 \mu\text{m} \times 1 \mu\text{m}$ to $20 \mu\text{m} \times 20 \mu\text{m}$ with different available aspect ratios. In the thesis, the further magnetic imaging analysis work was performed using the case studies of $20 \mu\text{m} \times 5 \mu\text{m}$ and $5 \mu\text{m} \times 20 \mu\text{m}$ geometries, due to the fact that the aspect ratio is preserved however the magnetization axis changes. The distance between each feature was $40 \mu\text{m}$ along each axis. The measurement procedure that was implemented having in mind the ability to perform 3D magnetic field reconstruction, by measuring the same sample four times applying different rotations to the sample stage. By measuring the sample four times where inbetween each measurement the stage angle is incremented by 90° , the sensitive axis of the sensor that remains fixed will measure the generated stray fields along different axes. This allows us to solve the measured field axis in order to the cartesian space magnetic field components (H_x, H_y, H_z) at each point separately in a linear system knowing the geometric transformations from the sensitive sensor axis to the laboratory frame.

D. Experimental Results

After establishing the procedures, the first experimental results were obtained. Nonetheless, the first acquisitions showed a large offset with a line dependent variation. In figure 7 we show examples of the

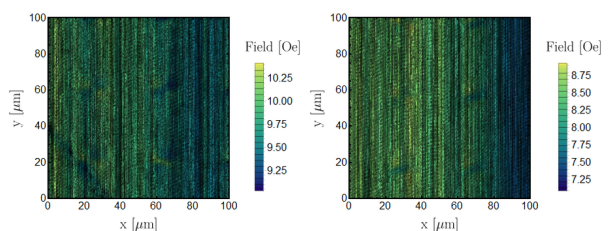


FIG. 7: Measured magnetic images for $5 \mu\text{m} \times 1 \mu\text{m}$ (left) $2 \mu\text{m} \times 2 \mu\text{m}$ CoFe features.

untreated data coming from the magnetic imaging setup. The impact of the noise is more visible for the weaker magnetic samples, almost completely covering the magnetic signal.

The strategy to remove this noise was based on a line by line fit of a linear function on the magnetic

imaging curve. Next, the resulting fit curve was then subtracted point by point from the data. With this approach, we were able to create a homogeneous background field around the magnetic patterns created by the magnetic features, indicating a successful removal of the magnetic offset, possibly created by adjacent electronic equipment. The results of this method are shown in figure 8.

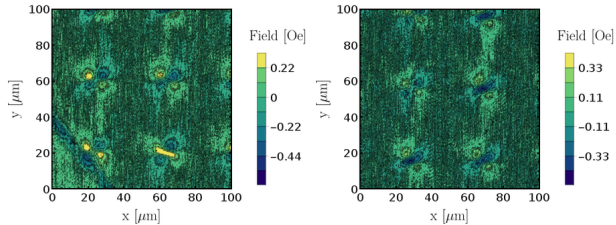


FIG. 8: Measured magnetic images for $5\mu\text{m} \times 1\mu\text{m}$ (left) $2\mu\text{m} \times 2\mu\text{m}$ CoFe features.

Additionally, successive iterations of linear fits were introduced, in order minimize the bias of the magnetic signal on the fit that is intended to remove the offset field. The method was successfully implemented, however we had difficulties to prove improved results, therefore for further data analysis, only first iteration offset removal fits were applied.

Furthermore, a random noise was observed, which was approached by the application of weighted averages of the intensity at the point with a certain neighboring region. Although the results showed a clear improvement in the visibility of patterns produced by small CoFe features, the intensity of the resulting magnetic images has questionable physical significance, thus this method would not be applied on the data for further studies.

V. SIMULATIONS AND VALIDATION

After removing major noise contributions introduced during acquisitions, we are able to compare measured magnetic imaging maps with simulated maps reproducing equivalent sample conditions. In the first run we noticed that the measured magnetic field patterns appeared to be slightly deviated when compared to the respective simulation results, which was assumed to be caused by a sample feature magnetization orientation slightly tilted from the x -axis. This observation motivated the implementation of an image overlay algorithm.

A. Magnetization Orientation Study

The algorithm will be based on the successive generation of simulated magnetic imaging maps with rotated magnetization orientation and comparison with the respective measured map. We identify the different magnetization orientations by introducing a nota-

tion analogous to the polar angles on the unit circle where a magnetization along the x -axis is associated with a $\phi_{\text{mag}} = 0^\circ$ angle and a magnetization along the y -axis will correspond to the angle $\phi_{\text{mag}} = 90^\circ$.

The approach is to recreate simulated magnetization intensity maps for magnetization angles between 0° and 350° in steps of 10° and subsequently overlay the results with the experimental measurements. The proximity of the simulation to the experiment is evaluated quantitatively by introducing a function that is based on running the sum of squared differences, meaning that we add the square of the differences between both amplitudes point by point and apply the square root over the sum. We divide the result by the total number of points n_{x_i, y_i} to eliminate the dependence on the considered sample size and to permit the interpretation of a mean deviation of simulation and measurement

$$f(\alpha, \phi_{\text{mag}}) = \frac{\sqrt{\text{SSD}(\alpha, \phi_{\text{mag}})}}{n_{x_i, y_i}}, \quad (4)$$

where $\text{Amp}_{\text{exp}}(x_i, y_i)$ is the measured magnetic intensity, $\text{Amp}_{\text{sim}}(\phi_{\text{mag}}, x_i, y_i)$ is the simulated magnetic intensity as a function of the sample magnetization angle and $n_{x_i, y_i} = n_{x_i} \times n_{y_i}$ is the number of points in \vec{e}_x and \vec{e}_y directions we are summing over. SSD is a notation used for sum of squared differences with $\text{SSD}(\alpha, \phi_{\text{mag}}) = \sqrt{\sum_{x_i, y_i} |\text{Amp}_{\text{exp}}(x_i, y_i) - (\alpha \text{Amp}_{\text{sim}}(\phi_{\text{mag}}, x_i, y_i))|^2}$. The parameter α is an additional degree of freedom we added to have the possibility to take into account or identify systematic amplitude deviations between simulations and experiment. The angle ϕ_{mag} that minimizes the function f is expected to reproduce more closely the measured magnetic field intensity maps.

One difficulty of the process is the positional overlay between measured intensity maps and the simulated ones with gradual magnetization rotation, since the measurement is started at an arbitrary position on top of the sample surface. As a result, the generation of simulation maps would have to be adjusted in the way that the simulated $100\mu\text{m} \times 100\mu\text{m}$ map would have the CoFe samples laying exactly at the same position as in the measured maps. The problem was approached by simulating larger areas of $200\mu\text{m} \times 200\mu\text{m}$, with the purpose of ensuring that inside this larger map there would be found a $100\mu\text{m} \times 100\mu\text{m}$ sized subregion with spacial conditions exactly identical to the ones found in the experiment. The matching position would be identified by placing the smaller measured map over the larger simulated map by evaluating the distance between both intensities at each point searching for a minimum. This procedure was performed by a integrated function of *Mathematica* [25], requiring a conversion of the intensity maps into monochromatic greyscale images, which renormalized the magnetic intensity values into colors ranging from 0 (black) to 1 (white). An example of this image overlay is presented in Fig. 9.

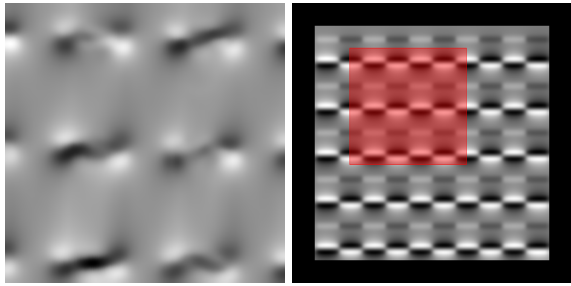


FIG. 9: Measured data greyscale image (left) and optimal overlay greyscale image for $20\mu\text{m} \times 5\mu\text{m}$ CoFe features.

In Fig. 9 we show a measured magnetic image converted into a greyscale image on the left and the larger simulated map with an area in red highlighting the optimal overlay position. Having generated the simulated maps occupying the same space as the measured data, we are able to apply the $f(\alpha, \phi_{\text{mag}})$ (4). function to identify which magnetization angle minimizes the difference between both amplitudes. To graphically summarize the sequence of the algorithm and highlighting the main steps and functions, we created a block diagram in Fig. 10.

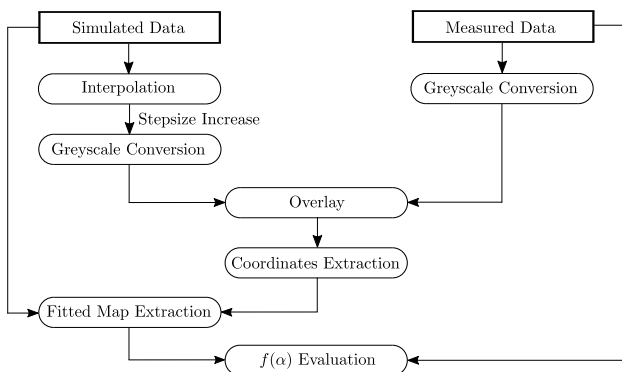


FIG. 10: Block diagram representation of the implemented magnetization rotation algorithm.

In this summarized version we will present the results for $20\mu\text{m} \times 5\mu\text{m}$ CoFe feature sample sizes at different stage angles ϕ . The function $f(\alpha, \phi_{\text{mag}})$ in equation (4) will compute the analogous of a vectorial Euler distance over a vector normalized by the number of elements. We decided to apply the function to the four stage angles simultaneously, as the angle of the stage does not affect the magnetization orientation. The minimization procedure of $f(\alpha, \phi_{\text{mag}})$ involves finding a minimum for each α and magnetization angle. The available ϕ_{mag} angles are already established by the step sizes chosen in the simulations with magnetization rotation. For the α parameter we have equally to evaluate the minimization using discrete values, ranging from -2 to 2 in 0.02 steps, as the computation of f at each point requires a time intensive sum operation over all available magnetic intensity amplitudes.

We firstly start by noting that in certain regions,

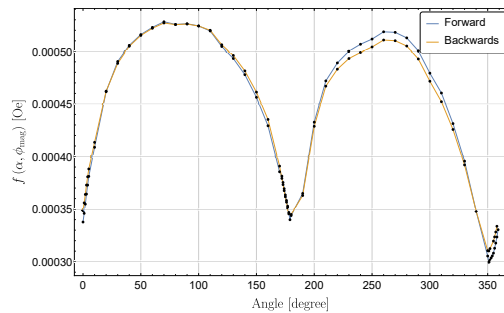


FIG. 11: Block diagram representation of the implemented magnetization rotation algorithm.

specifically around the $\phi_{\text{mag}} = 0^\circ$ and $\phi_{\text{mag}} = 180^\circ$ we reduced the magnetization rotation angular step size to 1° in order to obtain a higher resolution in the determination of the minimizing ϕ_{mag} angle.

Interpreting the results presented in Fig. 11, we can clearly observe that the sample magnetization angle evidently has an effect on the mean disparity between simulated and measured data. Nonetheless, the maximum and minimum values of the minimization function only differ by a factor of approximately 2, as the maximum value of the minimization routine lies above $f_{\text{max}}(\alpha, \phi_{\text{mag}}) \approx 5 \times 10^{-4}$ and the minimum close to $f_{\text{min}}(\alpha, \phi_{\text{mag}}) \approx 3 \times 10^{-4}$. This is given by the range of values we allow the variable α to take, as the maximum difference between measurement and simulation is capped by the amplitude of the measurement, thus whenever $\alpha = 0$, we expect that the distance between simulation and experiment to be larger than the experimental value itself, $|\text{Amp}_{\text{exp}}(x_i, y_i) - \text{Amp}_{\text{sim}}(x_i, y_i)| > |\text{Amp}_{\text{exp}}(x_i, y_i)|$.

As for each measurement we had access to two independent acquisitions, one during the forward movement of the cantilever and the other during the backward movement at each scanned line, we can compare the runs of the algorithm on both sets of data in order to evaluate the consistency of the obtained minimization. The results are presented in table,

Scanning Dir.	Min. (ϕ_{mag}) [$^\circ$]	Min. ($f(\alpha, \phi_{\text{mag}})$) [10^{-4} Oe]
Forward	351	2.99
Backwards	351	3.10

TABLE II: Results of the $20\mu\text{m} \times 5\mu\text{m}$ magnetization rotation study

Tab. V A shows good agreement between both acquisitions, indicating that the magnetization of the sample features was deviated by 9° in the clockwise direction from the x -axis of the laboratory frame. After being able to identify the magnetization orientation of the measured magnetic samples, the simulated magnetic imaging maps returned pattern shapes with good similarity to the respective measured counterparts, giving us good confidence when using the simulated maps as auxiliary tool for the evaluation of the

measured data.

B. Field component decomposition

One integral part of this work is the decomposition of the magnetic field intensity measured by the sensor into its cartesian laboratory frame components $\{H_x, H_y, H_z\}$. The basic procedure to perform the decomposition is by using the magnetic imaging scans at the four different stage angles and solve the system as a set of linear equations

$$\begin{cases} B_{\text{sens}_{0^\circ}} &= -B_y \times \cos(10^\circ) - B_z \times \sin(10^\circ) \\ B_{\text{sens}_{90^\circ}} &= -B_x \times \cos(10^\circ) - B_z \times \sin(10^\circ) \\ B_{\text{sens}_{180^\circ}} &= B_y \times \cos(10^\circ) - B_z \times \sin(10^\circ) \\ B_{\text{sens}_{270^\circ}} &= B_x \times \cos(10^\circ) - B_z \times \sin(10^\circ), \end{cases} \quad (5)$$

where the 10° angle is related to the cantilever tilt. The angles at the index of a sensed field B_{sens_ϕ} describe the measured field along the cantilever axis with a rotation ϕ applied to the sample stage. The positioning of the cantilever relative to the sample stage for each angle ϕ is represented in figure 12. The sensi-

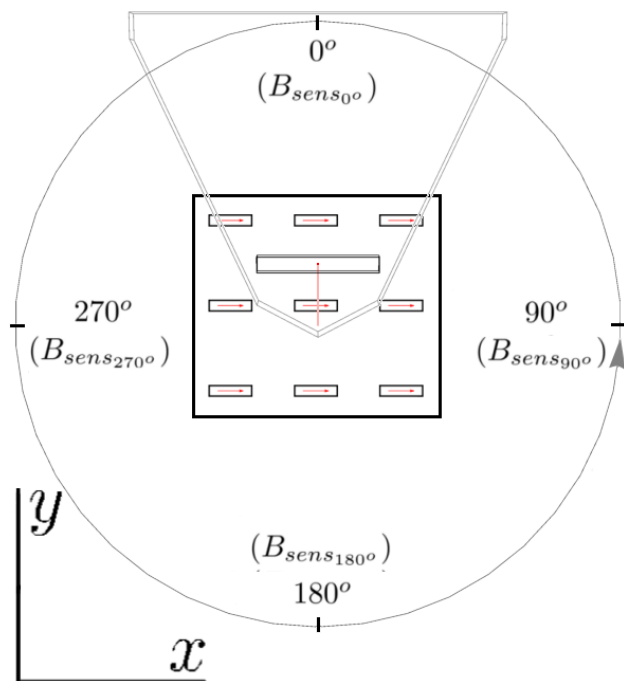


FIG. 12: Stage orientation for decomposition measurements

tive orientation is given by the orientation of the red line leaving the center of the sensor.

Having the measured fields at the same point in space along different stage angles we are able to solve for the three cartesian components. Nonetheless, equally as in the previous section, the initial obstacle was related to the fact that each measurement starts in an arbitrary position on the sample. To be able

to apply (5) point by point, we need to ensure that the measured field intensities B_{sens_ϕ} for the stage angles $\phi = \{0^\circ, 90^\circ, 180^\circ, 270^\circ\}$ are consistent in their positioning relative to the magnetic features, so the approach was by considering again a subregion of the magnetic field intensity map. In this context, the only reasonable subregion was isolating the magnetic field pattern created by a single CoFe feature, where the limit in each direction was the mid distance to the center of the next pattern. The center of a field pattern was determined by consulting the respective topography images, however, as already discussed, due to dust particle contamination of the samples it was not possible to automatize the position extraction, therefore the center of a magnetic feature on each scan was identified manually. We remind that the center of a feature in the topography scans and the magnetic scans are deviated by an offset of $11.4 \times \cos(10^\circ) \mu\text{m}$ along the cantilever long axis, due to the fact that the sensor does not lie on the center of the AFM tip, which had to be compensated when extracting the coordinates of the magnetic pattern centers.

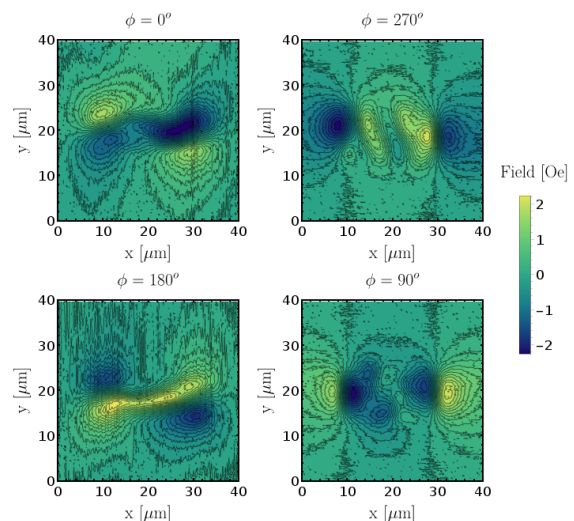


FIG. 13: Single pattern isolation for field decomposition on a $20\mu\text{m} \times 5\mu\text{m}$ feature sample.

The result of the single pattern isolation for a $20\mu\text{m} \times 5\mu\text{m}$ sized feature occupying a $40\mu\text{m} \times 40\mu\text{m}$ area is presented in Fig. 13.

Having the magnetic intensities organized in equally sized maps and equivalent spacial coordinates on the laboratory frame, we are able to perform a the field intensity decomposition for each point.

In Fig. 14 we show the results of the magnetic field decomposition. On the upper left image we can see the H_x component, on the upper right image the H_y component, on the lower left the H_z component and on the lower right we present a stray field line reconstruction at the sensor height by combining the results from the H_x and H_y components. In the original thesis these results are compared to the simulations together with an interpretation of the field pattern shapes.

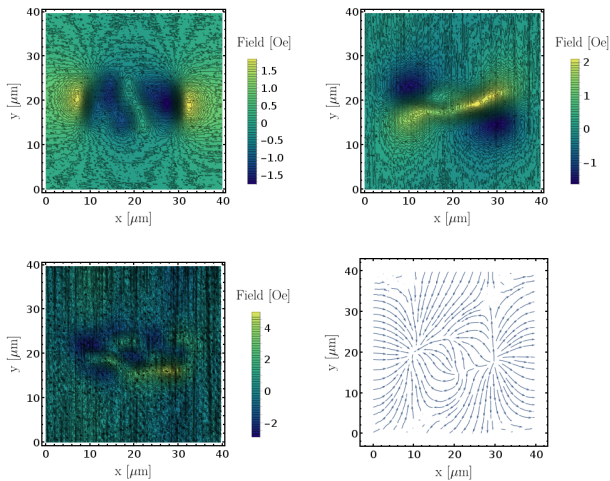


FIG. 14: $20\mu\text{m} \times 5\mu\text{m}$ CoFe feature magnetic field reconstruction.

VI. CONCLUSIONS

In this work performed the characterization of a previously developed and assembled SMRM setup, including electronic and mechanical calibrations with evaluation of the effects each of the available parameters had on the resulting magnetic imaging map out-

put.

By the introduction of a numerical description of the device output immersed in the magnetic stray fields created by arrays of differently sized patterned stacks with a ferromagnetic CoFe layer, a tool was provided to assist the evaluation and interpretation of the experimental results, starting with the identification of a tilt magnetization orientation due to mismatch between the measured magnetic field patterns and the predictions provided by the simulated maps.

Joining the results of the previous sections, we were able to successfully perform a 3D-field reconstruction by measuring each sample along four different sensitive directions, allowing transform the measured magnetic field intensities measured at each point into the magnetic field components along the three cartesian axes (H_x, H_y, H_z) in the laboratory frame. The same process was replicated by the corresponding simulated maps taking into account the magnetization orientation corrections. As future work, we suggest the development of next sensor generations in order to evaluate the performance of the simulation tools with other sensor geometries and dimensions, specially regarding the performance of the magnetic field reconstruction tool, which we expect to have improved performances with more balanced aspect ratios, eventually achieved by current perpendicular to plane devices.

-
- [1] K. L. Kelly, E. Coronado, L. L. Zhao, G. C. Schatz, *et al.*, *Journal of Physical Chemistry B-Condensed Phase* **107**, 668 (2003).
- [2] A. Albanese, P. S. Tang, and W. C. Chan, *Annual review of biomedical engineering* **14**, 1 (2012).
- [3] L. Vila, T. Kimura, and Y. Otani, *Physical review letters* **99**, 226604 (2007).
- [4] K. Matsuyama, H. Asada, S. Ikeda, and K. Taniguchi, *IEEE Transactions on Magnetics* **33**, 3283 (1997).
- [5] K. Inomata, *IEICE transactions on electronics* **84**, 740 (2001).
- [6] S. X. Wang and G. Li, *IEEE transactions on Magnetics* **44**, 1687 (2008).
- [7] O. V. Salata, *Journal of nanobiotechnology* **2**, 3 (2004).
- [8] S. I. Stoeva, F. Huo, J.-S. Lee, and C. A. Mirkin, *Journal of the American Chemical Society* **127**, 15362 (2005).
- [9] X. Qian, X.-H. Peng, D. O. Ansari, Q. Yin-Goen, G. Z. Chen, D. M. Shin, L. Yang, A. N. Young, M. D. Wang, and S. Nie, *Nature biotechnology* **26**, 83 (2008).
- [10] M. Costa, J. Gaspar, R. Ferreira, E. Paz, H. Fonseca, M. Martins, S. Cardoso, and P. P. Freitas, *IEEE Transactions on Magnetics* **51**, 1 (2015).
- [11] A. Fert and I. A. Campbell, *Journal of Physics F: Metal Physics* **6**, 849 (1976).
- [12] M. D. Stiles, *Journal of Applied Physics* **79**, 5805 (1996), <http://aip.scitation.org/doi/pdf/10.1063/1.362195>.
- [13] J. Nogués and I. K. Schuller, *Journal of Magnetism and Magnetic Materials* **192**, 203 (1999).
- [14] C. H. Tsang, R. E. Fontana, T. Lin, D. E. Heim, B. A. Gurney, and M. L. Williams, *IBM Journal of Research and Development* **42**, 103 (1998).
- [15] S. C. P. P. Freitas, R. Ferreira and F. Cardoso, *Journal of Physics: Condensed Matter* (2007).
- [16] L. Neel, *Comptes Rendus* **255**, 1676 (1962).
- [17] S. S. P. Parkin, N. More, and K. P. Roche, *Phys. Rev. Lett.* **64**, 2304 (1990).
- [18] G. Binnig, H. Rohrer, C. Gerber, and E. Weibel, *Phys. Rev. Lett.* **49**, 57 (1982).
- [19] H.-J. Butt, B. Cappella, and M. Kappl, *Surface Science Reports* **59**, 1 (2005).
- [20] Q. Zhong, D. Inniss, K. Kjoller, and V. Elings, *Surface Science* **290**, L688 (1993).
- [21] J. M. Neumeister and W. A. Ducker, *Review of Scientific Instruments* **65**, 2527 (1994), <http://dx.doi.org/10.1063/1.1144646>.
- [22] S. Magonov, V. Elings, and M.-H. Whangbo, *Surface Science* **375**, L385 (1997).
- [23] S. ichi Kitamura and M. Iwatsuki, *Japanese Journal of Applied Physics* **34**, L145 (1995).
- [24] M. Costa, J. Gaspar, F. Richeimer, S. Cardoso, and P. Freitas, in *Scanning magnetoresistance microscopy enabled by AFM cantilevers with integrated magnetic sensors*, edited by M. 2016 (Micro and Nano Engineering, 2016).
- [25] W. Research, “Mathematica 10,” (2015).
- [26] E. P. Furlani, *Permanent magnet and electromechanical devices: materials, analysis, and applications*, edited by Elsevier (Academic press, 2001).